First-principles study of electronic structure, transport, and optical properties of $EuCd_2As_2$

Jyoti Krishna, T. Nautiyal, and T. Maitra
Department of Physics, Indian Institute of Technology, Roorkee, Roorkee 247667, Uttarakhand, India

(Received 30 March 2018; revised manuscript received 9 July 2018; published 6 September 2018)

Recent experimental measurements on the layered triangular-lattice antiferromagnet $EuCd_2As_2$ have revealed an interesting interplay among magnetism, charge transport, and optical properties. To explore the nature of the interaction among these degrees of freedom, the electronic structure, magnetic properties, electrical transport, and optical properties of $EuCd_2As_2$ are investigated using density functional theory and Boltzmann transport theory under various approximations such as the generalized gradient approximation (GGA), GGA+U, and GGA+U+spin orbit (SO). A semimetallic electronic structure with compensating electron and hole pockets is observed. Among the various magnetic states studied, A-type antiferromagnetic (A-AFM) and ferromagnetic (FM) states emerge as having competing total energies even though A-AFM is found to be energetically favored. Further, our GGA+U+SO calculations reveal the presence of a magnetic anisotropy which drives the spin moments to align along the crystallographic b direction. We observe from our transport calculations that in the case of A-AFM, the anisotropy between out-of-plane and in-plane resistivities (ρ_{zz}/ρ_{xx}) is much higher than that in the FM case, and it increases as temperature goes down, exactly what has been observed experimentally for this system. The huge difference between the resistivities of A-AFM and FM states at lower temperatures is indicative of the presence of negative magnetoresistance in the system as seen in the experimental measurements. In-plane optical reflectivity reveals that intraband contributions play a major role in reproducing the experimental features in the low-frequency regime.

DOI: 10.1103/PhysRevB.98.125110

I. INTRODUCTION

Recently, much attention has been paid to the layered intermetallic compounds containing magnetic ions where a strong interplay between magnetism and charge transport properties makes these materials conducive for device applications in areas such as spintronics, thermoelectrics, etc. A subset of these materials, europium-based 122 pnictides (with $CaAl_2Si_2$-type structure), possesses localized magnetic moments on a triangular lattice where geometric frustration of the underlying lattice coupled with strong Coulomb correlation and spin-orbit coupling brings in novel antiferromagnetic phases which can be tuned easily with externally applied magnetic field [1–3]. It has also been reported very recently that these materials can host symmetry-protected nontrivial topological phases such as a Dirac semimetallic state [2–4].

Many layered 122-type AM_2X_2 ternary intermetallic compounds belong to the family of Zintl phases, which can crystallize favorably into $ThCr_2Si_2$- (tetragonal) type structure and, rarely, into $CaAl_2Si_2$ (trigonal) type; the formation of latter is restricted to certain specific conditions [5]. $ThCr_2Si_2$-type [6,7] compounds have been widely studied in the field of high-T_C superconductivity, the most common being ternary Fe-based pnictides [8]. Often, these compounds tend to be antiferromagnetic [9], and superconductivity emerges due to doping or under high pressures [8]. On the other hand, $CaAl_2Si_2$-type compounds have applications mostly in thermoelectrics. In the prototype $CaAl_2Si_2$, both electrons and holes contribute to the electrical transport properties [10,11].

These compounds show extremely rich magnetic properties. Considerable research has been carried out to reveal the magnetic properties of compounds with $CaAl_2Si_2$-type structure and their Mn-doped variants [12–15]. This paper is mainly focused on $EuCd_2As_2$ (Fig. 1), a $CaAl_2Si_2$-type compound. Recent experimental investigations show that in this compound, $Eu^{2+}(4f^7)$ ions contribute to long-range magnetic order and offer strong scattering to the conducting carriers from Cd and As [1,16].

Experiments further show that $EuCd_2As_2$ undergoes a magnetic transition from the paramagnetic phase to the antiferromagnetic phase on lowering the temperature. A positive Weiss constant from the susceptibility curve indicates the ferromagnetic fluctuations in the paramagnetic regime [16]. Wang *et al.* [1] recently studied the variation of in-plane (ρ_{ab}) and out-of-plane (ρ_c) resistivity with temperature in the presence of magnetic field. They observed that in the case of zero magnetic field, the resistivity shows a remarkable increase with the decrease in temperature close to the magnetic transition until a peak is attained at 9.5 K, which marks an antiferromagnetic (AFM) transition temperature, below which resistivity decreases again with temperature. However, the anisotropy in the resistivity ρ_c/ρ_{ab} keeps increasing even below the AFM transition temperature. From these observations, the authors [1] conjectured the magnetic ground state is an A-type AFM (with Eu moments aligned in an antiparallel manner along the c-direction) as there is higher scattering along the c direction than in the ab plane due to antiferromagnetic ordering. Very recent experimental measurements of resonant elastic x-ray scattering [2] indeed observed the system to be A-type AFM. However, this study finds the spin moments to lie in the ab plane rather than along the c axis (which was proposed to be the case by Wang *et al.*). Further, Wang *et al.*

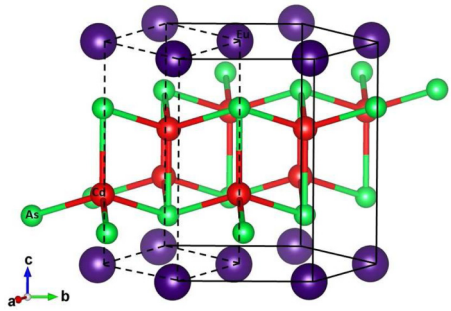

FIG. 1. Hexagonal crystal structure of $EuCd_2As_2$ (space group $P\bar{3}m1$). As (green) and Cd (red) form a double-corrugated hexagonal layer [10] sandwiched between Eu (violet) atoms. The dashed lines denote the unit cell.

reported that when the system is exposed to a magnetic field along the c direction, no resistivity peak is observed, and the anisotropy in resistivity is reduced as well, indicating high negative magnetoresistance in this system. In addition to the charge transport properties, Wang *et al.* [1] also studied the in-plane optical properties which indicate the semimetallic nature of this compound. Very recently, it was also reported that $EuCd_2As_2$ displays the properties of a Dirac semimetal [2,4]. To understand the experimental observations discussed above which indicate a strong interplay among the magnetic, charge transport, and optical properties in this system, an exhaustive theoretical calculation is warranted. Therefore, in this work, we investigate the electronic structure, magnetic, charge transport, and optical properties of this system in detail from a theoretical perspective using first-principles density functional theory.

II. METHODOLOGY

The structural parameters were taken from experiments [16]. The electronic structure calculations were carried out using *ab initio* density functional theory with the Perdew-Burke-Ernzerhof generalized gradient approximation (PBE-GGA) [17] exchange-correlation functional within the full potential linearized augmented plane-wave method as implemented in WIEN2K [18]. Because of the presence of highly localized f electrons of Eu, both Coulomb correlation U and spin-orbit (SO) interaction were included in our calculations through GGA+U and GGA+U+SO. The GGA+U approximation takes into account the on-site Coulomb interaction and removes the self-Coulomb and self-exchange-correlation energy. The spin-orbit coupling (SOC) is included by the second variational method with scalar relativistic wave functions. For self-consistent field calculations, 896 $\vec{k}$ points were considered in the irreducible Brillouin zone, and the plane-wave cutoff ($R_{mt}K_{\max}$) was set to 7.0 for all the calculations. The muffin-tin radii were taken to be 2.5 a.u. for Eu/Cd and 2.49 a.u. for As. Plane-wave expansion in spherical harmonics was considered up to angular momentum quantum number $l = 10$. Transport properties were calculated within Boltzmann transport theory with the constant-relaxation-time approximation as implemented in BOLTZWANN [19]. This uses maximally localized Wannier functions (MLWFs) as basis functions which are generated by fitting the density functional theory bands calculated by WIEN2K with MLWFs. WANNIER90 [20] and WIEN2WANNIER [21] codes were used for this purpose. For proper convergence of the quantities related to the transport properties that are evaluated, we have used a dense k mesh of $40 \times 40 \times 40$, which is necessary because of the steepness of the Fermi-Dirac distribution near the Fermi energy. For the optical properties, we have employed a fine k mesh of 60 000 $\vec{k}$ points in the full Brillouin zone.

III. RESULTS AND DISCUSSION

A. Electronic structure and magnetic order

We performed the basic electronic structure calculations by considering various magnetic configurations of Eu spin moments (see Fig. 2), i.e., ferromagnetic (FM), A-type antiferromagnetic (A-AFM), C′-AFM, and G′-AFM in addition to the nonmagnetic (NM) case, where Eu spin moments are set to zero. For A-AFM we further considered the cases where Eu spin moments are pointed along the crystallographic **b** and Cartesian **x** axes in addition to the case where they point along the crystallographic **c** axis. C′-AFM and G′-AFM states are found to be energetically much higher than FM and A-AFM. Therefore, we list in Table I the total energies calculated under various approximations for the FM and various A-AFM configurations considered. We note that the NM solution is higher in energy by about 7 eV with respect to the magnetic solutions (AFM/FM) and therefore is not included in Table I. From the total energies presented in Table I, we note that FM and A-AFM configurations are energetically quite close to each other within all the approximations considered. GGA gives the ferromagnetic configuration as the lowest-energy state. Application of U narrows the energy difference between the FM and A-AFM states drastically, with FM being favored by only 0.24 meV for $U_{\text{eff}} = U - J = 3$ eV (where U is the Coulomb correlation and J is Hund's exchange). On increasing U further, at $U_{\text{eff}} = 5$ eV A-AFM becomes the ground-state magnetic configuration. A-AFM consistently remains the preferred phase even after inclusion of the SOC. We find the A-AFM configuration with spin moments aligned along **b** to have the lowest energy, although FM is found to be energetically quite close. The magnetic anisotropy energy is calculated to be 1.4 meV per formula unit. A very recent experimental measurement on this system also observed the spin moments to lie in the ab plane [2]. In Table II we present the energy difference between A-AFM and FM as a function of U. We clearly observe that the ground state changes from FM to A-AFM as U increases. With the increase in the U value the position of localized $4f$ states of Eu is also pushed further below the Fermi level (FL).

In Figs. 3(a)–3(c), we present the partial density of states (DOS) for NM, FM, and A-AFM within GGA, respectively. It is clearly seen that highly localized europium f states ($4f^7$) lie just below the Fermi level and there are highly delocalized (or itinerant) states of Cd s, As p, and Eu d characters crossing the Fermi level. From DOS plots, the NM state is clearly seen to be metallic, whereas very low DOS seems to be present at the FL in the case of FM and A-AFM. Since Eu f electrons are strongly correlated, we have performed GGA+U calculations for FM and A-AFM magnetic configurations at

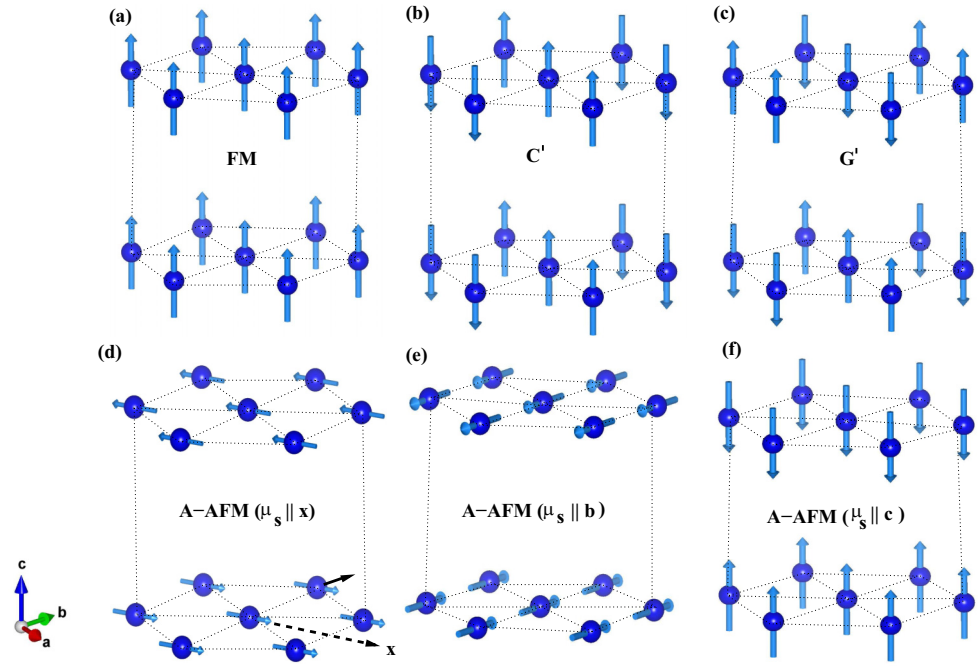

FIG. 2. Various magnetic orders considered in our calculation: (a) ferromagnetic (FM), (b) C′-AFM, and (c) G′-AFM. The bottom row shows A-AFM with moments along (d) **x**, (e) **b**, and (f) **c**.

U_{eff} = 3, 4, and 5 eV. We present in Fig. 4 the orbital projected DOS for A-AFM calculated within GGA+U with U_{eff} = 5 eV. Figure 4 shows that with the application of U, the f states are pushed to ∼1.0 eV below the FL. At U_{eff} = 5 eV the system still shows a semimetallic nature as a few bands continue to intersect the FL [see Fig. 5(c)]. However, on increasing U further, the system becomes insulating. Note that in Figs. 3(c) and 4 exactly equal DOSs in the spin-up and -down sectors are seen because of the presence of an equal number of up- and down-spin electrons in the A-AFM phase.

To get a clearer picture of the states near the FL, we calculated the band structure for both majority (up, hereafter UP) and minority (down, hereafter DN) spin states. Figure 5(a) represents the same calculated within GGA for FM plotted along the high-symmetry directions. Clearly, a few bands do cross the FL, giving rise to the semimetallic character as observed experimentally for this system. In the UP spin sector, three bands (1, 2, and 3) are seen to cross the FL; one creates a hole pocket in the A-Γ direction (band 1), and another (band 3) creates a large electron pocket centered at A and a very small one at M. In Figs. 5(b) and 5(c) we present the band structures for FM and A-AFM calculated within GGA+U with U_{eff} = 3 eV and U_{eff} = 5 eV, respectively. We can clearly see that the number of bands crossing the FL decreases with the increase in the U value, and localized Eu f states are pushed farther below FL. In Fig. 6 we present the Fermi surface calculated for A-AFM within GGA, where we can clearly see the electron and hole pockets at A and Γ, respectively. These Fermi pockets are seen to shrink in size on inclusion of U and U+SO (not shown here).

TABLE I. Total energy per formula unit (in meV) of FM and A-AFM magnetic configurations within different exchange-correlation functionals (XC), calculated with reference to the lowest-energy state for each approximation. M denotes the magnetization direction.

XC	FM	A-AFM
GGA	0	2.94
GGA+U		
U_{eff} = 3 eV	0	0.24
U_{eff} = 5 eV	0.51	0
GGA+U+SO,		
U_{eff} = 5 eV		
$M \parallel x$ axis	2.94	2.62
$M \parallel b$ axis	0.31	0
$M \parallel c$ axis	1.75	1.40

B. Transport properties

Transport properties of $EuCd_2As_2$ have been calculated under the constant-relaxation-time approximation within the Boltzmann transport theory. Figure 7 shows in-plane (ρ_{xx}) and out-of-plane (ρ_{zz}) resistivity variation with temperature for the A-AFM and FM cases within GGA. We can see that resistivity along the c axis (i.e., out of plane) is always greater than the in-plane one in both cases, the difference being significantly

TABLE II. Variation of the energy difference between A-AFM and FM ΔE with respect to U_{eff}.

	U_{eff} (eV)			
	0	3	5	7
ΔE (meV)	2.94	0.24	−1.50	−209.4

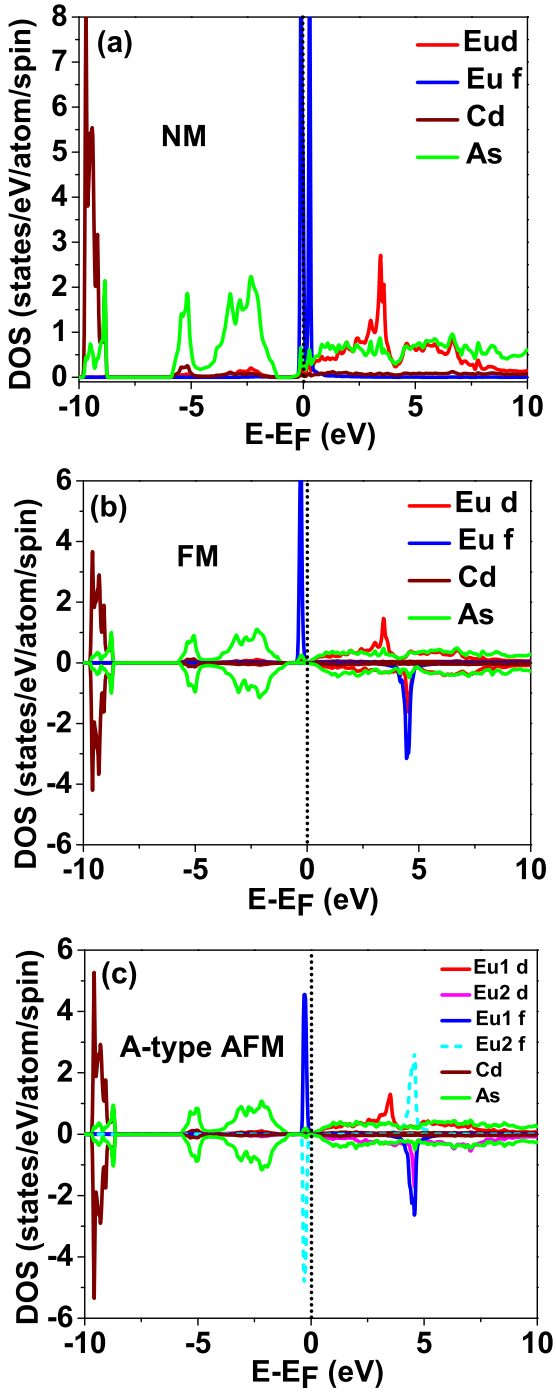

FIG. 3. Partial DOS for (a) NM, (b) FM, and (c) A-type AFM within GGA. The negative values for DOS represent the DOS for the down-spin channel. Eu f and Cd DOS are scaled down by a factor of 6 to make As p and Eu d states visible. In (c) for A-type AFM, the f DOSs of Eu1 and Eu2 are shown in different colors to depict the spin polarization of Eu f states. Here the Eu1 ion is in the configuration with net spin being up, and Eu2 is in the configuration with net spin being down within A-AFM.

large in the case of A-AFM. Based on the observation of higher resistivity along the c direction from their transport measurements, Wang *et al.* [1] proposed the magnetic ground state is A-AFM. Although our total energy calculations show that A-AFM and FM states have competing energies (see

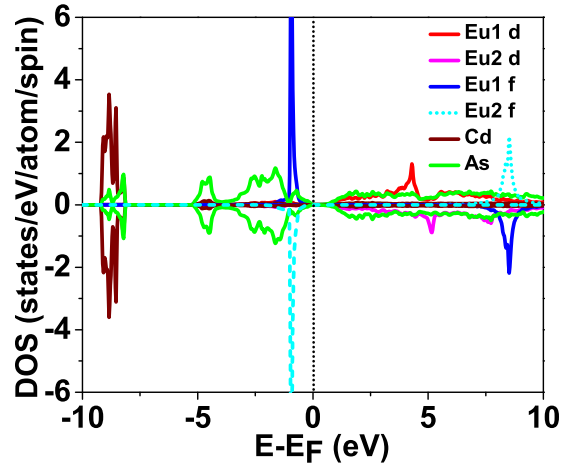

FIG. 4. Partial DOS for A-type AFM within GGA+U with $U_{\text{eff}} = U - J = 5$ eV. Eu f and Cd DOS are scaled down by a factor of 6 to make As p and Eu d states visible. The f DOSs of Eu1 and Eu2 are shown in different colors to depict the spin polarization of Eu f states. Here the Eu1 ion is in the configuration with net spin being up, and Eu2 is in the configuration with net spin being down within A-AFM.

Table I), calculated transport properties of A-AFM match well with those observed experimentally. We further notice that in the FM case, the resistivity is almost independent of temperature, whereas in A-AFM it increases with the lowering of the temperature.

At low temperatures, we see a huge difference (an order of magnitude) in resistivities of A-AFM and FM states, the latter being much smaller. This drop (which is equivalent to the system being exposed to an external magnetic field which causes the Eu spins to align along one particular direction, the c direction in this case) indicates the presence of negative magnetoresistance as also observed experimentally for this system [1]. At higher temperatures, metallic conductivity (resistivity shows a positive slope with an increase in temperature) is seen with a slight change in the chemical potential μ, as illustrated in the inset of Fig. 7.

Evaluation of the anisotropy ratio $\frac{\rho_{zz}}{\rho_{xx}}$ reflects the amount of scattering along different directions; hence, its dependence on temperature has also been studied for FM and A-AFM, as shown in Fig. 8. We clearly see that for A-AFM, $\frac{\rho_{zz}}{\rho_{xx}}$ increases with a decrease in temperature, whereas in the case of FM the ratio decreases. This is exactly what is observed in experiment as well [1]. To analyze the origin of such a large difference between the anisotropy ratios in FM and A-AFM at low temperature, we analyzed the corresponding band structures and calculated the associated transport velocities of the charge carriers along three different directions, as shown in the inset of Fig. 8 for A-AFM. Indeed, we observe that the transport velocities of charge carriers along the Γ-A direction (i.e., the c direction) are much smaller than those in the other two directions (i.e., in the ab plane).

C. Optical properties

In view of the optical measurements reported by Wang *et al.* [1], we calculated the optical properties from *ab initio*

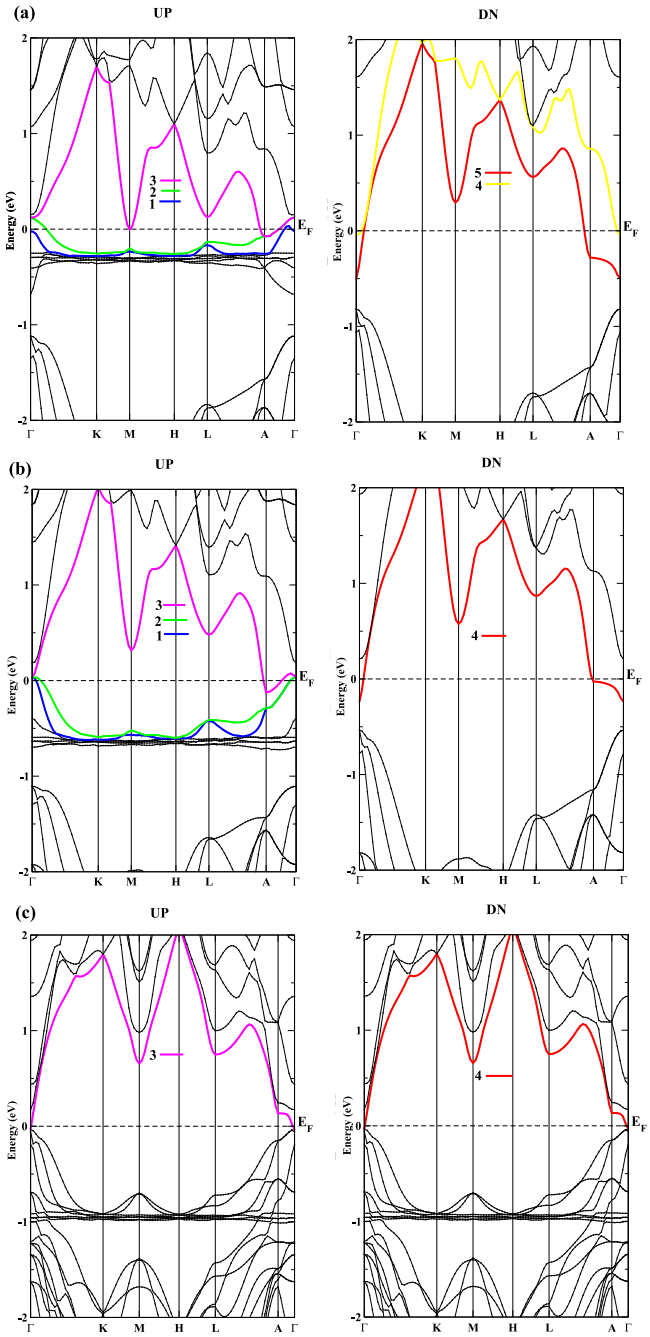

FIG. 5. Band structure plots for FM within (a) GGA and (b) GGA+U with $U_{\text{eff}} = 3$ eV and (c) for A-AFM with $U_{\text{eff}} = 5$ eV in the UP (majority) and DN (minority) spin channels. The bands crossing the Fermi level are shown in color.

density functional theory calculations within the GGA, GGA+U, and GGA+U+SO approximations. We focused on FM and A-AFM magnetic configurations as these two states have competing energies. The electronic structure discussed earlier clearly indicates that $EuCd_2As_2$ has a semimetallic character with a few bands crossing the Fermi level, giving rise to small electron and hole pockets in certain high-symmetry directions of the Brillouin zone. Due to the semimetallic nature of the compound, we have considered the intraband contribution in addition to the interband transitions

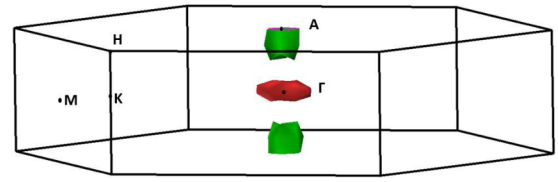

FIG. 6. Fermi surface of A-AFM within GGA showing electron pockets at A (green) and hole pockets at Γ (red).

for the estimation of the optical response functions. Very fine Drude and Lorentz broadening of the order of 10^{-3} eV has been considered for the entire energy range of frequencies to clearly see the effect of intraband transitions which are prominent only at lower frequencies and die off rapidly as the photon frequency increases.

We have calculated the in-plane (XX) and out-of-plane (ZZ) optical reflectivity $R(\omega)$ as a function of incident photon frequency ω in the FM and A-AFM phases within the GGA, GGA+U, and GGA+SO+U approximations. A clear anisotropy is observed in $R(\omega)$ between the XX and ZZ (not shown here) components. To compare our results with the experiments by Wang *et al.* [1] in which they measured the in-plane behavior, we present the in-plane optical reflectivity calculated within various approximations as mentioned above. Figure 9(a) shows $R(\omega)$ versus ω calculated for the FM state within GGA and GGA+U with $U_{\text{eff}} = 3$ eV and for A-AFM with $U_{\text{eff}} = 5$ eV as these are the corresponding ground-state magnetic orders. At lower frequencies, $R(\omega)$ approaches unity, in agreement with experimental observations. On increasing the frequency, $R(\omega)$ shows a peak followed by a dip characterizing the plasma frequency. This behavior indicates a metallic response of the system. Figure 9(a) provides a logarithmic plot to encompass the behavior at higher frequencies as well. For $U_{\text{eff}} = 5$ eV [Fig. 9(a)], the plasma peak appears at $\sim 137\,\text{cm}^{-1}$, in excellent agreement with the corresponding peak, seen just below 220 cm^{-1} in the experimental measurements (see Fig. 4(a) of Ref. [1]). At lower U values this peak shifts towards higher frequencies. By comparing the frequency dependence with that measured experimentally, we

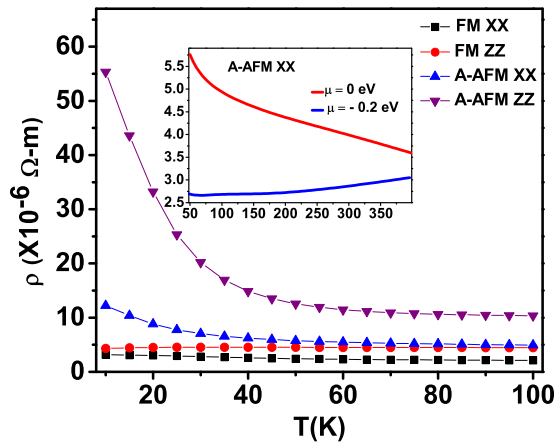

FIG. 7. In-plane and out-of-plane ρ vs T plots for A-AFM and FM, showing ρ_{zz} is always higher in all cases. The inset shows the ρ_{xx} of A-AFM for chemical potential $\mu = 0.0$ eV (red) and $\mu = -0.2$ eV (blue) as a function of T.

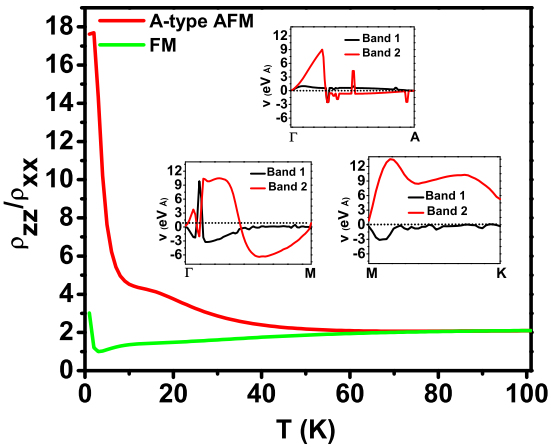

FIG. 8. Anisotropy ratio ρ_{zz}/ρ_{xx} vs T (K) for A-AFM and FM. The inset shows electron and hole velocities in different directions for the two bands crossing the FL.

observe that our results with $U_{\text{eff}} = 5$ eV, i.e., for the A-AFM phase, compare better with the experiment.

To study the effect of SO coupling on optical reflectivity $R(\omega)$, we have considered the A-AFM state with the magnetization along [1, 0, 0] [parallel to x-axis, see Fig.2(d)], [0, 1, 0], and [0,0,1] and $U_{\text{eff}} = 5$ eV. Figure 9(b) shows $R(\omega)$ within GGA+U+SO for all three directions of magnetization. A pronounced anisotropy is seen at lower frequencies (below 600 cm^{-1}) between the cases with magnetization in the ab plane and along the c direction. However, higher-

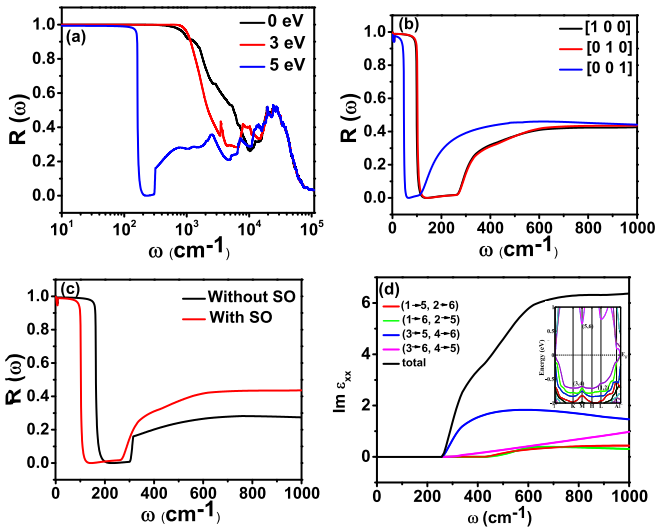

FIG. 9. In-plane $R(\omega)$ vs ω (in cm^{-1}). (a) Plot in logarithmic scale of the FM state within GGA and GGA+U ($U_{\text{eff}} = 3$ eV) and for the A-AFM state ($U_{\text{eff}} = 5$ eV) as FM is the ground-state magnetic order within GGA and GGA+U with $U_{\text{eff}} = 3$ eV, whereas A-AFM is the ground state at $U_{\text{eff}} = 5$ eV. (b) The effect of SO coupling on $R(\omega)$ with the magnetization axis along [1, 0, 0], [0, 1, 0], and [0,0,1] for the A-AFM state with $U_{\text{eff}} = 5$ eV. (c) $R(\omega)$ without and with SO for A-AFM with the magnetization axis along [0,1,0] and $U_{\text{eff}} = 5$ eV. (d) Imaginary part of the in-plane dielectric function showing contributions from interband transitions for A-AFM calculated for GGA+U+SO with $U_{\text{eff}} = 5$ eV and the magnetization axis along [0,1,0]. The inset shows the corresponding band structure.

frequency $R(\omega)$ spectra show similar behavior for magnetization along different directions. Plasma frequency for magnetization along [0,1,0] is found to be 143 cm^{-1}, whereas it is 66 cm^{-1} for [0,0,1]. Plasma frequency is determined by the frequency at which the real part of the dielectric function goes to zero. Thus, magnetization along [0,1,0] has close agreement with the experimental plasma frequency. Comparing this with results without SO [see Fig. 9(c)], we find that the plasma frequency is reduced slightly with the inclusion of SO. The plasma frequency without SO is found to be 229 cm^{-1}, whereas it reduces to 143 cm^{-1} with the inclusion of SO owing to fewer states being occupied compared to the case without SO. Nevertheless, a small plasma frequency in all cases is indicative of the fact that the compound is semimetallic with very small occupation of states near the FL, in agreement with experiment [1].

In order to understand the anisotropy seen in the optical reflectivity with respect to the change in the magnetization direction [Fig. 9(b)], we analyze the contribution of the individual interband transitions to the optical reflectivity. We compute [shown in Fig. 9(d)] the imaginary part of the in-plane dielectric function versus frequency for A-AFM with magnetization along b. We observe that the dominant contribution in this case comes from the interband transitions $3 \rightarrow 5$ and $4 \rightarrow 6$ [the inset of Fig. 9(d) shows the corresponding band structure]. Due to the strong dependence of the band structure around the FL on the magnetization direction, the corresponding interband transition contributions also get affected (not shown here) and lead to the anisotropy seen in Fig. 9(b).

D. Conclusions

Using first-principles density functional theory calculations, we have studied the electronic structure, magnetic ground-state, electrical transport, and optical properties at various levels of approximations, which include Coulomb correlation within GGA+U and spin-orbit interaction within GGA+U+SO. Our total energy calculations for various magnetic configurations such as FM, A-AFM, and NM revealed that FM and A-AFM have competing total energies within GGA, GGA+U, and GGA+U+SO. Electronic band structure calculations indicate the semimetallic nature of $EuCd_2As_2$ with compensating electron and hole pockets along certain high-symmetry directions. These Fermi pockets are mainly composed of As p and Cd s states. The semimetallic nature persists even after including the Coulomb correlation, although the size of the Fermi pockets decreases. The calculated transport properties indicate that the anisotropy in the resistivities (ρ_c/ρ_{ab} or equivalently ρ_{zz}/ρ_{xx}) is much higher in the case of A-AFM than in FM and becomes much more pronounced as the temperature goes down, replicating the experimental behavior. Therefore, one can conclude that A-AFM is a more likely ground-state magnetic order of this system. However, we observed from our GGA+U+SO calculations that there is magnetic anisotropy in this system which drives spin moments to align along the crystallographic **b** direction as opposed to the **c**-direction moment alignment proposed by Wang *et al.* [1]. The frequency dependence of in-plane optical reflectivity indicates that intraband contributions to optical reflectivity play a significant role in the low-frequency region

in addition to interband contributions. We also observed that a strong Coulomb correlation of about 5 eV is required to reproduce the features observed experimentally along with the correct plasma frequency.

ACKNOWLEDGMENT

J.K. acknowledges Ministry of Human Resource Development (MHRD), India, for a research fellowship.

[1] H. P. Wang, D. S. Wu, Y. G. Shi, and N. L. Wang, Phys. Rev. B **94**, 045112 (2016).

[2] M. C. Rahn, J.-R. Soh, S. Francoual, L. S. I. Veiga, J. Strempfer, J. Mardegan, D. Y. Yan, Y. F. Guo, Y. G. Shi, and A. T. Boothroyd, Phys. Rev. B **97**, 214422 (2018).

[3] J.-R. Soh, C. Donnerer, K. M. Hughes, E. Schierle, E. Weschke, D. Prabhakaran, and A. T. Boothroyd, Phys. Rev. B **98**, 064419 (2018).

[4] G. Hua, S. Nie, Z. Song, R. Yu, G. Xu, and K. Yao, arXiv:1801.02806.

[5] H. Zhang, J.-T. Zhao, Y. Grin, X.-J. Wang, M.-B. Tang, Z.-Y. Man, H.-H. Chen, and X.-X. Yang, J. Chem. Phys. **129**, 164713 (2008).

[6] H. Mizoguchi, T. Kuroda, T. Kamiya, and H. Hosono, Phys. Rev. Lett. **106**, 237001 (2011).

[7] I. R. Shein and A. L. Ivanovskii, Solid State Commun. **151**, 1165 (2011).

[8] P. L. Alireza, Y. T. C. Ko, J. Gillett, C. M. Petrone, J. M. Cole, G. G. Lonzarich, and S. E. Sebastian, J. Phys.: Condens. Matter **21**, 012208 (2009).

[9] K. A. Filsinger, W. Schnelle, P. Adler, G. H. Fecher, M. Reehuis, A. Hoser, J.-U. Hoffmann, P. Werner, M. Greenblatt, and C. Felser, Phys. Rev. B **95**, 184414 (2017).

[10] M. Imai, H. Abe, and K. Yamada, Inorg. Chem. **43**, 5186 (2004).

[11] X.-J. Wang, M.-B. Tang, H.-H. Chen, X.-X. Yang, J.-T. Zhao, U. Burkhardt, and Y. Grin, Appl. Phys. Lett. **94**, 092106 (2009).

[12] K. Zhao, B. J. Chen, Z. Deng, W. Han, G. Q. Zhao, J. L. Zhu, Q. Q. Liu, X. C. Wang, B. Frandsen, L. Liu, S. Cheung, F. L. Ning, T. J. S. Munsie, T. Medina, G. M. Luke, J. P. Carlo, J. Munevar, G. M. Zhang, Y. J. Uemura, and C. Q. Jin, J. Appl. Phys. **116**, 163906 (2014).

[13] A. C. Payne, A. E. Sprauve, M. M. Olmstead, S. M. Kauzlarich, J. Y. Chan, B. A. Reisner, and J. W. Lynn, J. Solid State Chem. **163**, 498 (2002).

[14] Y. Goryunov, V. Fritsch, H. V. Lohneysen, and A. Nateprov, J. Phys.: Conf. Ser. **391**, 012015 (2012).

[15] A. Maurya, R. Kulkarni, A. Thamizhavel, P. Bonville, and S. K. Dhar, J. Phys.: Conf. Ser. **592**, 012045 (2015).

[16] I. Schellenberg, U. Pfannenschmidt, M. Eul, C. Schwickert, and R. Pottgen, Z. Anorg. Allg. Chem. **637**, 1863 (2011).

[17] J. P. Perdew, A. Ruzsinszky, G. I. Csonka, O. A. Vydrov, G. E. Scuseria, L. A. Constantin, X. Zhou, and K. Burke, Phys. Rev. Lett. **100**, 136406 (2008).

[18] P. Blaha, K. Schwarz, G. K. H. Madsen, D. Kvasnicka, J. Luitz, R. Laskowski, F. Tran, and L. D. Marks, *WIEN2K, An Augmented Plane Wave + Local Orbitals Program for Calculating Crystal Properties* (Karlheinz Schwarz, Techn. Universitat Wien, Austria, 2018).

[19] G. Pizzi, D. Volja, B. Kozinsky, M. Fornari, and N. Marzari, Comput. Phys. Commun. **185**, 422 (2014).

[20] A. A. Mostofi, J. R. Yates, Y.-S. Lee, I. Souza, D. Vanderbilt, and N. Marzari, Comput. Phys. Commun. **178**, 685 (2008).

[21] J. Kunes, R. Arita, P. Wissgot, A. Toschi, H. Ikeda, and K. Held, Comput. Phys. Commun. **181**, 1888 (2010).